# Finite element analysis and experimental verification of high reliability synchronous reluctance machine

Indexed by:
Web of Science Group

Wiesław Łyskawinski [a], Cezary Jędryczka [a], Dorota Stachowiak [a,*], Piotr Łukaszewicz [a], Michał Czarnecki [b]

[a] Poznan University of Technology, Faculty of Control, Robotics and Electrical Engineering, ul. Piotrowo 3A, 60-965 Poznań, Poland
[b] Department of Renewable Energy Sources, Falenty, Al. Hrabska 3, 05-090 Raszyn, Poland

## Highlights

- Development of the numerical model of SynRM exploiting the finite element method.
- Confirming reliability of the model on basis of experimental and simulation studies.
- Determining parameters of the equivalent circuit of the SynRM basing on the field model.

## Abstract

The aim of this study was to investigate and analyse the synchronous reluctance machine. An accurate method for determining the lumped parameters of an equivalent circuit of the studied machine has been proposed. The method is based on the phase currents and voltages analysis at low slip operation. Experimental research of a synchronous reluctance machine is supplemented by simulation studies. The field-circuit model of electromagnetic phenomena in the considered motor was developed and used in simulation. The proposed method allows the numerical model to be verified by comparing the calculated and measured torque-angle characteristics of the machine. The test results obtained are presented and discussed. Achieved satisfactory concordance between simulation and experiment results proves that the proposed approach can be useful in the synthesis of reliable synchronous reluctance machines as well as in their control systems.

## Keywords

synchronous reluctance motor, measurement methods, finite element analysis, equivalent circuit.

## 1. Introduction

In research related to development and analysis of reliable technical solutions the field models, due to their credibility, are being increasingly used. Among others the finite element method become widely used in modeling of variety of technical devices [50]. Due to its versatility FEM has been successfully employed for solving complex problems, among others for modeling magneto-optics for the aircraft skins inspections [7] in stress simulations for fatigue life prediction of a radial cylindrical roller bearing [6] as well as to study temperature and strain fields in gas-foil bearings [47] and modeling a deep-hole boring tool [15]. The multi-domain approach for modeling pantograph-catenary interaction has been discussed in [48] while mechanical behavior of cork-rubber pads for vibration isolation exploiting FEM has been proposed by [19]. Numerical models exploiting FEM are also applied to study of electromagnetic phenomena in electrical machines. The field and field circuit models exploiting FEM have been successfully applied in analysis and synthesis of many different types of electromechanical transducers, as induction [3, 8] and synchronous machines [4, 25], switched reluctance motors [35],

stepper motors [38], brushless direct current machines [11, 30], levitation systems (linear motors) [31] as well as in wireless power transfer systems [17], magnetic field excitation systems [23] and other electromagnetic converters.

Due to high reliability and low manufacturing costs [20, 22], as well as dynamic development in the field of power electronic converters and complex control algorithms [28, 29], in many research teams around the world more and more attention is paid to synchronous reluctance machine (SynRM) [9]. From the point of view of mechanical design, with respect to the commonly used squirrel-cage induction machines, SynRM machines differ in the rotor construction. The rotor of SynRM machines is made in the form of a steel sheet laminated magnetic circuit characterized by a large asymmetry of reluctance in the direct and quadrature axis of the machine. In the classical SynRM machine, the rotor is without cage winding, which significantly reduces the cost of production and increases the reliability of the machine.

Due to their features, SynRM's are proposed to be used in harsh operating conditions requiring high reliability and robustness of electric motors. Hence, these motors are increasingly used in electric vehicle

(*) Corresponding author.
E-mail addresses: W. Łyskawinski (ORCID: 0000-0002-6483-3322): wieslaw.lyskawinski@put.poznan.pl, , C. Jędryczka (ORCID: 0000-0001-5427-059X): cezary.jedryczka@put.poznan.pl, D. Stachowiak (ORCID: 0000-0002-6245-963X): dorota.stachowiak@put.poznan.pl, P. Łukaszewicz (ORCID: 0000-0002-1169-3282): piotr.lukaszewicz@put.poznan.pl, M. Czarnecki (ORCID: 0000-0002-9223-8934): m.czarnecki@itp.edu.pl

drives [1, 46] , aviation [32] pumps [10], traction [26], fans , cranes, compressors etc.

In terms of the operating principle, SynRM machines are synchronous machines in which the speed does not depend on the load torque but is determined by the supply frequency and the number of pole pairs of the stator windings. In practice, this means that SynRM machines do not develop a starting torque when directly connected directly to the grid. Consequently, in order to enable starting and operation over a wide speed range, it is necessary to power this type of machine through appropriately controlled power electronic converter systems.

In order to increase the reliability of electric drives powered by power electronic converter systems, intensive research on multiphase machines is being conducted in many research and development centers around the world [12, 41, 45]. Increasing the number of phases, and thus the converter branches allows to reduce the phase currents of the machine it means also currents in the switching transistors of the inverter. As it was demonstrated in [13, 14], the use of multiphase solutions allows the ensure proper operation of the machine in under the supply system faults conditions. The research on multiphase SynRM machines is in its early stages and requires, due to the complexity of their control algorithms [40, 42, 44], the development of reliable models of the electromagnetic phenomena occurring. The use of field [16] and field-circuit models [17] due to the precise representation of electromagnetic phenomena allows to obtain reliable results [49]. Unfortunately, calculations using field models based on FEM are very time-consuming and therefore not possible to implement directly in control systems of SynRM. In practice, lumped parameter models based on equivalent circuits are used in control algorithms [2, 37]. Their advantage is low computational complexity. Unfortunately, the reliability of the representation of phenomena by equivalent circuit models can be questionable when parameters of these model will be not verified by experiments or more accurate field-circuit models.

The research on the advance control algorithms as well as the optimal design of the motor magnetic circuit are the two main streams that help to increase the efficiency and reliability of SynRM based drives [5, 9, 36]. Research conducted on the subject has led to the development of several SynRM rotor designs starting from adapted IM rotor laminations to the single or multi-flux barriers topologies [27, 34]. In addition to the radial flux rotor designs, an axial fluxSynRM concept has also been proposed [24, 33]. To design the new SynRM rotor structures, researchers initially used a simplified mathematical analysis [18, 43].

Given the promising future of SynRM, it is worthwhile to improve both the analytical as well as numerical models and conduct simulation and experimental studies of these motors. Of great importance in the developed numerical models is the reliability of the obtained results. In order to verify these results correctly, it is important to develop reliable measurement methods to ensure accurate and repeatable measurement results.

For these reasons, the paper attempts to develop a numerical model of the SynRM machine allowing for the determination of the parameters of the equivalent scheme. The reliability of the developed model was confirmed by experimental tests. The proposed method to determine the parameters of the equivalent scheme based on the field model can be effectively implemented in research on the synthesis of multiphase SynRM machines.

## 2. Field model of SynRM

A three-phase M3AL 100LB 4 synchronous reluctance motor with a power of 3 kW was used in this study. The rotor of this motor features a modern four-pole structure with magnetic barriers (Figure 1). The outer cylindrical surface of this rotor and the small air gap between the rotor and the stator core ensure low dissipation flux and idle current. Therefore, the efficiency of these motors is similar or even better than induction motors [29].
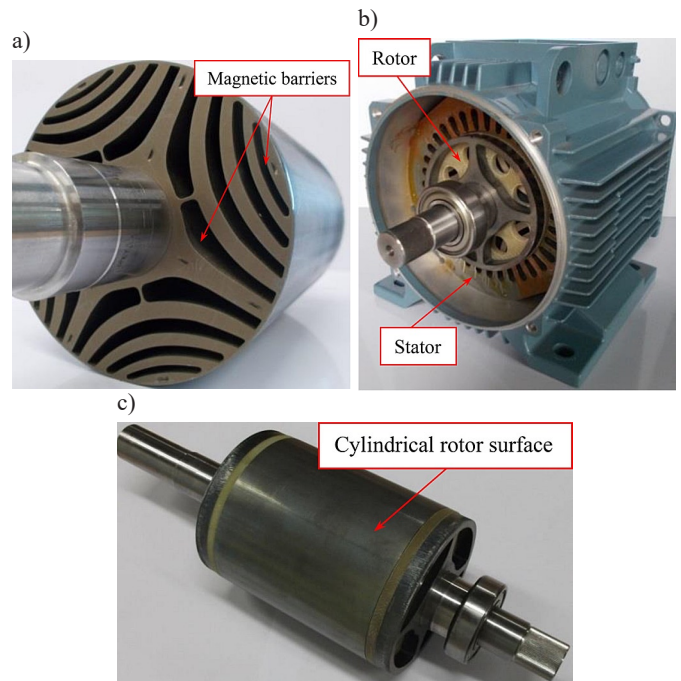


*Fig. 1. Rotor of the test motor: (a) rotor with magnetic barriers, (b) front view of the stator and rotor in the outer casing, (c) outer cylindrical rotor surface*

In further research, a field model of the motor under consideration was developed. In the analysis of SynRM machines, due to the strong influence of the core nonlinearity, field models based on the Finite Element Analysis (FEM) are commonly used [21, 31]. The use of advanced simulation techniques reduces the cost and time of building and testing motor prototypes. The field model of the tested SynRM was developed in ANSYS - Maxwell environment (Figure 2). The parameters of the analysed motor are listed in Table 1.

Parametric models were developed to allow modification of the main dimensions of the magnetic circuit of the machine (rotor and stator diameters, stator slot and rotor magnetic barriers geometry. Due to the symmetry of the magnetic circuit, a model reduced to 1/4 of the
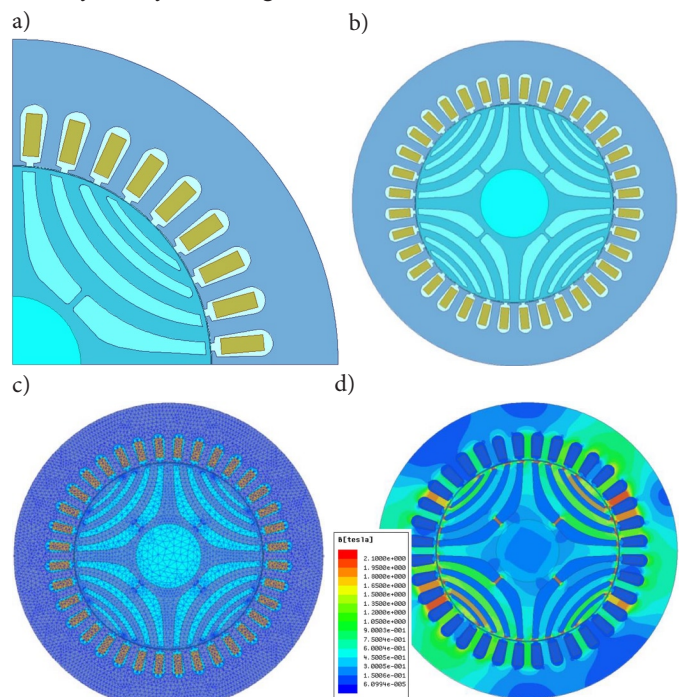


*Fig. 2. Field model of studied SynRM: (a) reduced geometry, (b) full geometry model, (c) applied finite element mesh and (d) magnetic flux density plot at chosen time instant and load angle*

*Table 1. Parameters of considered Synchronous Reluctance Motor*

| Parameter | Value | Parameter | Value |
|---|---|---|---|
| Rated power | 3 kW | Stator outer diameter | 170 mm |
| Rated speed | 1500 rpm | Stator inner diameter | 104 mm |
| Rated current | 7.1 A | Rotor shaft diameter | 31 mm |
| Rated voltage | 380 V | Rotor outer diameter | 103.4 mm |
| Number of phases | 3 | Air gap length | 0.3 mm |
| Number of slots | 36 | Active axial length | 110 mm |
| Number of poles | 4 | Stator steel | M270-50A |
| Number of rotor flux barriers per pole | 3 | Rotor steel | M270-50A |
| Frequency | 50 Hz | Number of turns per coil | 33 |
| Main winding resistance | 1.6 Ω | Winding wire diameter | 2x0.8 mm |

where: $I_{max}$, $I_{min}$ are maximum and minimum values of the current and $U_{max}$, $U_{min}$ are maximum and minimum values of the voltage determined from acquired voltage and current waveforms (Figure 4); $R_a$ is armature winding resistance, which, with a change of temperature, is described by the relation $R_a=R_o[1+\alpha(T-T_o)]$ where $R_o$ is armature winding resistance in ambient temperature, $T_o$, $T$ are the ambient and armature winding temperatures, respectively, $\alpha$ is the temperature coefficient that determines the relative increase in resistance when the temperature increases by 1 K (for Cu $\alpha$=0.004 1/K).
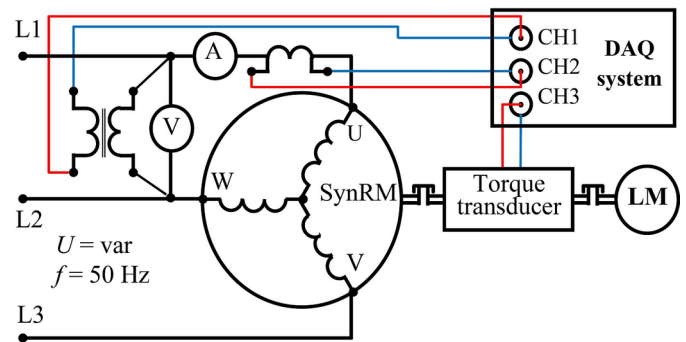
machine geometry was developed (Figure 2a). Such a model, with appropriate discretization of the considered area, ensures obtaining correct results of simulation calculations for the dynamic states of the analysed motor in acceptable time. Reliability of this model was confirmed by comparing the results obtained in the method of low slip from measurements and calculations. For steady-state analysis, a field model developed for the full magnetic circuit of the motor under study can be used (Figure 2b). The mesh discretizing the machine area is shown in Figure 2c, while exemplary magnetic field distribution is presented in Figure 2d. The full geometry model was adapted to determine the torque-angle characteristics $T(\beta)$ by simplified method discussed in section 4.3.

*Fig. 3. Schematic diagram of the measuring system for determining synchronous reactances by the low slip method*

## 3. Experimental verification

### 3.1. Low-slip method

According to the adopted method, the rotor of the tested motor is driven at a speed close to synchronous, at which the slip should not be greater than 0.01. The three-phase armature winding placed in the stator slots is supplied with a reduced voltage (Figure 3) of such a value that the rotor will not fall into synchronism under the influence of the reluctance torque. The direction of rotation of the magnetic field created by the current in the armature winding should be consistent with the rotor rotation direction. The difference in rotor speed and stator magnetic field causes a change in position of the direct axis $d$ and the quadrature axis $q$ of the rotor with respect to the stator field axis. Appropriate forming of magnetic barriers in the rotor ensures small permeance $\Lambda$ for the armature reaction flux in the quadrature axis $q$ and large permeance in the direct axis $d$. For the above reasons, the armature reaction reactance ($X = 2\pi f N^2\Lambda$; where $N$ is the number of armature winding turns), and hence the synchronous reactance in the range from $X_d$ to $X_q$, changes periodically with a doubling of the slip frequency $f$. A change in this reactance causes a periodic sweep of current in the armature winding with a doubling of the slip frequency. These changes in current cause changes in the voltage drop across the internal impedance of the power source, resulting in periodic fluctuations in the supply voltage to the motor under test. In order to determine the reactances $X_d$ and $X_q$, the maximum and minimum values of the voltage and current supplying the motor must be measured. During measurements of the tested motor, these values were calculated from the recorded waveforms of the supply voltage and current in the armature winding as well as using digital meters with the memory of the maximum and minimum values of voltage or current. Based on the measurement results, the reactances $X_d$ and $X_q$ are calculated from the following relation [39]:

$$X_d = \sqrt{\frac{U_{max}^2}{3I_{min}^2} - R_a^2} \quad X_q = \sqrt{\frac{U_{min}^2}{3I_{max}^2} - R_a^2} \quad (1)$$

If the voltage does not reach extreme values at the largest and smallest current values, the voltage values occurring at the same instant as the current values $I_{max}$ and $I_{min}$ should be taken. The reactances $X_d$ and $X_q$ are calculated for several different slips and then by extrapolation these reactances are determined at slip equal to zero. Recorded voltage and current waveforms are shown in Figure 4.
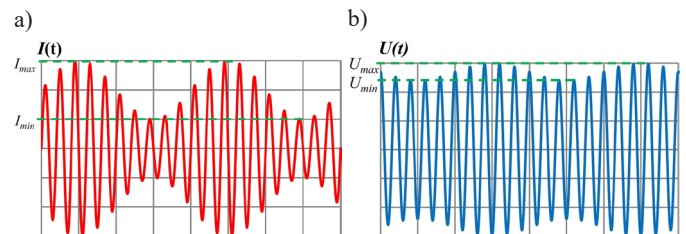
*Fig.4. Current (a) and voltage (b) waveforms in the SynRM armature winding from the low slip method*

### 3.2. Test rig method

In further studies, the external characteristics were determined, i.e. the dependence of the electromagnetic torque $T$ as a function of the internal load angle $\beta$ (power angle). In order to calculate this torque in the tested SynRM it is necessary to determine the values of the reactance $X_d$ and $X_q$ according to the described method of low slip. For this purpose, the test rig shown in Figure 5 was built. The tested motor was connected to the dynamometer via a torque transducer enabling measurement of load torque $T$ and speed $n$. The motor was supplied from an autotransformer, which provided a regulated three phase voltage of value (80 - 200 V). In a dynamometer with much higher torque than the tested motor, the rotational speed was set slightly lower than the synchronous speed. To measure voltages and currents, digital meters with memory for peak values (maximum and minimum voltages and currents supplying the tested motor) and power analyser were used. Voltage and current waveforms were acquired by data acquisition system composed of current and voltage transducers, PCI multichannel analog to digital converter provided by National Instruments and LabVIEW software.
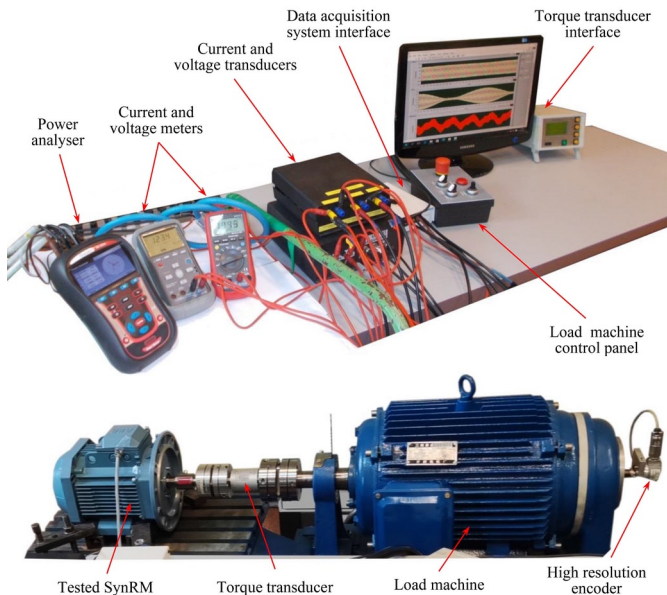
Fig.5. Experimental setup and equipment for SynRM tests

## 4. Comparison of experimental and simulation results

### 4.1. Comparison of direct reactance Xd and quadrature reactance Xq determined by measurements and simulations using the low slip method

The quadrature and direct synchronous reactances (Figure 6) determined by measurements ($X_{dm}$, $X_{qm}$) and simulations ($X_{dc}$, $X_{qc}$) were compared in the course of the conducted tests. These reactances were calculated from relation (1) at different rotor speeds $n$ (slips $s = (n_s - n) / n_s$) near the synchronous speed $n$. During the measurements, the rotor speed was forced by the set speed in the dynamometer (Figure 5). Minimum and maximum values of currents and voltages were read from meters storing extreme values. These values were also determined on the basis of waveforms obtained by FEM simulations. Selected waveforms of voltages and currents recorded during measurements and simulations at slip $s = 0.004$ (speed $n = 1494$ rpm) are shown in Figure 7. The waveforms were recorded at phase-to-phase voltage $U = 100$ V set before powering SynRM.
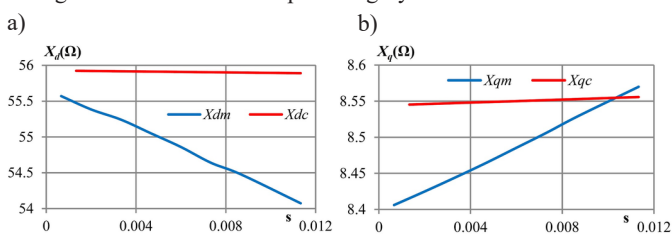


Fig. 6. Direct reactances $X_d$ (a) and quadrature reactances $X_q$ (b) determined as a function of slip $s$ (subscript m for reactances determined by measurements; subscript c for reactances determined by FEM simulations)

Extrapolating determined values of the synchronous reactances for a slip equal to zero (synchronous speed $n_s$), the external characteristics (torque-angle) of the SynRM were determined by the following formula:

$$T = \frac{3}{2\omega_s} U_{ph}^2 \left( \frac{1}{X_q} - \frac{1}{X_d} \right) \sin 2\beta \qquad (2)$$

The external characteristics are compared in Figure 8, taking into account in relation (2) the rated phase voltage $U_{ph} = 230$ V of the
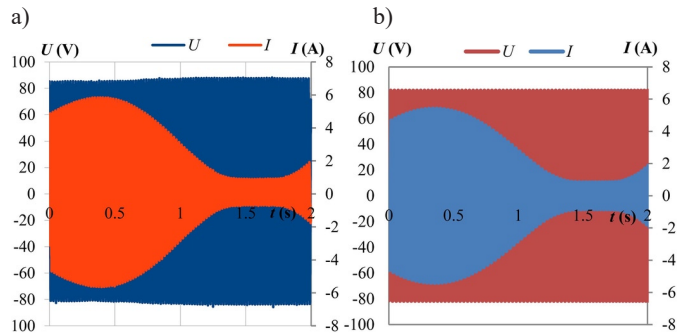


Fig. 7. Current and voltage waveforms obtained by: (a) measurements and (b) simulations in the low slip method at n = 1494 rpm

tested SynRM, its synchronous angular velocity $\omega_s$ and determined by measurements and simulations of the direct reactance $X_d$ and quadrature reactance $X_q$ of the slip $s = 0$ according to the method of low slip. The maximum difference between the two characteristics occurs at the maximum torque $T_{max}$, i.e. for the power angle of 45° and 135° (Figure 8). The maximum percent difference of these characteristics can be calculated from the expression:

$$\delta_{max} = \left| \frac{T_{m\,max} - T_{c\,max}}{T_{m\,max}} \right| 100 \qquad (3)$$

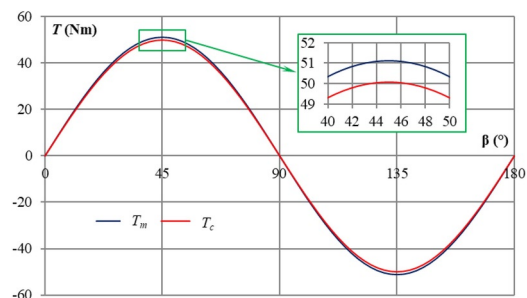For the considered external characteristics $\delta_{max} = 2.05$ %.



Fig. 8. Torque T as a function of power angle β ($T_m$ determined on the basis of measurements, $T_c$ determined on the basis of FEM simulations)

### 4.2. Influence of supply voltage

In order to reliably validate the field model of SynRM, the effect of voltage on the lumped parameters of the considered machine was investigated. The maximum and minimum currents were determined at the given mains voltages supplying the tested SynRM. The dependencies of these currents on the voltage supplying the SynRM obtained for the speed $n = 1494$ rpm are shown in Figure 9. Noticeable discrepancies between the measurement and simulation results in the maximum values of currents may be related to the insufficient stiffness of the load machine torque vs. angle characteristic observed during the measurements. For this reason, tests were not continued at higher voltage values because the reluctance torque increasing with the square of the voltage caused the rotor to be pulled into synchronism.

In a similar manner as described earlier, the direct and quadrature reactances were determined for different values of the supply voltages of the armature windings of the SynRM under test. Assuming that the reactance of the windings $X = 2\pi f L$ is dependent on the frequency $f$ and the inductance $L$ of these windings, the direct and quadrature inductances can be calculated for frequency $f = 50$ Hz. The results obtained of reactances and inductances as a function of voltage are shown in Figure 10.

To highlight the discrepancy between measurement and calculations, the direct axis $d$ and the quadrature axis $q$ inductances and reactances have been compared in separate plots (see Figure 11 (a) to (d)).
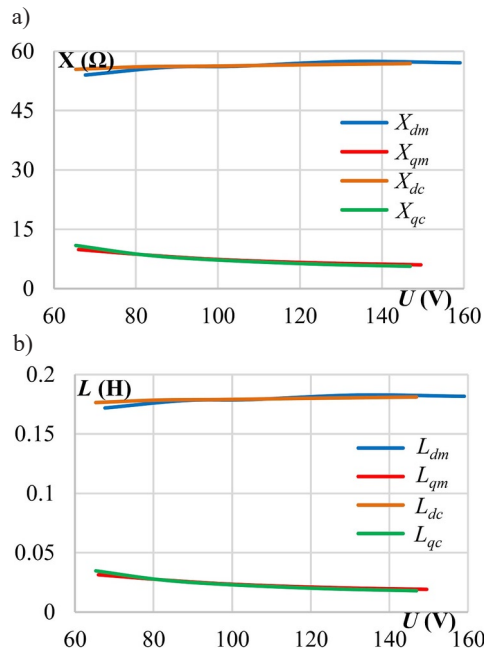
Fig. 9. Values of (a) maximum and (b) minimum currents as a function of armature winding supply voltage determined by measurements ($I_{maxm}$, $I_{minm}$) and obtained by simulations ($I_{maxc}$, $I_{minc}$) at $n = 1494$ rpm
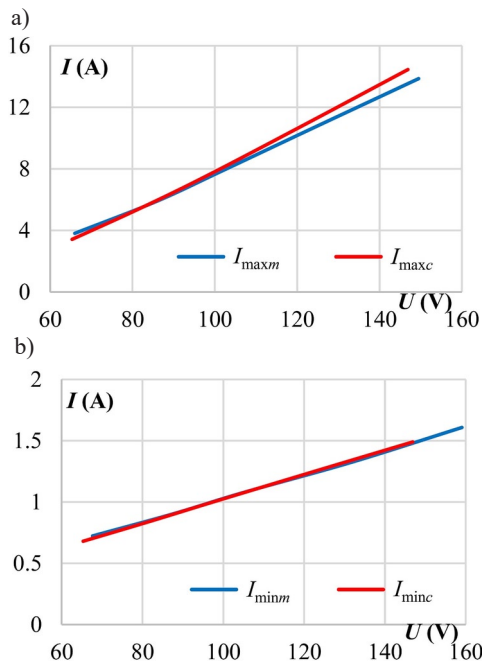


Fig. 10. Reactances (a) direct $X_d$ and quadrature $X_q$ and inductances (b) direct $L_d$ and quadrature $L_q$ determined as a function of voltage $U$ on the armature winding

## 4.3. Torque-angle characteristics

It has been demonstrated that the proposed low-slip method allows reliably validate the field model for different voltages. However, at higher voltages the problem of pulling the rotor into synchronism during measurements arises. The elimination of this problem requires the use of an appropriately oversized dynamometer in relation to the electromagnetic torque of the tested motor in order to prevent the rotor from being pull into synchronicity. Besides, it should be emphasized that simulation calculations for the method of low slip are very time-consuming. The calculation of one variant for a given voltage and rotor speed takes about 6 h on an HP Z800 Workstation Intel®Xeon(R) W5580 3.20 GHz 64 GB computer. For this reason, an alternative method of determining the torque-angle characteristics was examined.
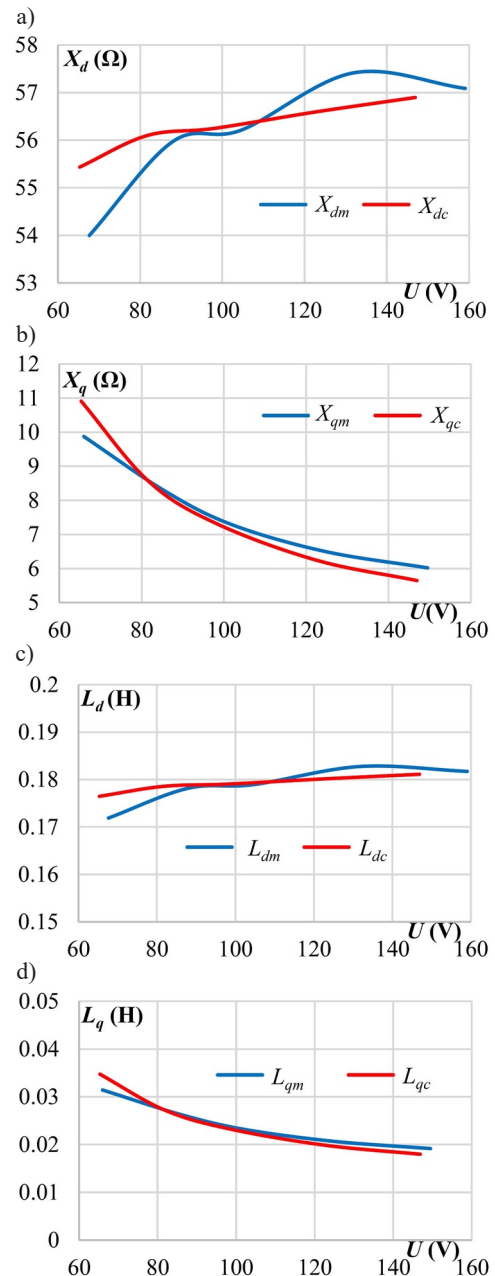


Fig. 11. Reactances (a) direct $X_d$ and (b) quadrature $X_q$ and inductances (c) direct $L_d$ and quadrature (d) $L_q$ determined as a function of voltage $U$ on the armature windings

In studied method, the torque generated by the SynRM at a given rotor position and different values of phase currents in the armature windings is determined. The phase currents are forced by the three programmable DC supplies according to its sinusoidal variation during real motor operation. In other words, the torque-angle characteristic is measured at zero speed and "locked" rotor position by changing the stator magnetomotive force vector position. Selected torque-angle characteristics determined according to discussed method are shown in Figure 12. It should be noted that at different rotor positions the maximum and minimum values of torque differs significantly. The reason of observed offsets of torque-angle characteristics is occurrence, in addition to the main reluctance torque originating from the rotor magnetic circuit asymmetry, torques caused by the slotting of the stator, i.e. produced by higher spatial harmonics of the magnetic reluctance distribution related to the position of the rotor in respect to the stator slots.

Our study shows that experimental verification allows the use discussed simplified "forced current" method to determine torque vs. angle characteristics. Nevertheless, it should be highlighted that despite
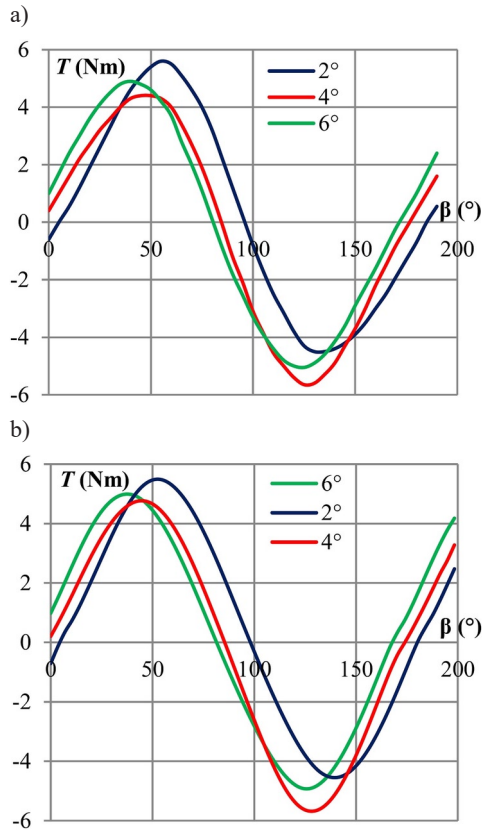
a)



b)



*Fig. 12. Torque-angle characteristics of the tested SynRM under sinusoidal forced DC current in the armature windings determined by: (a) measurements and (b) calculations for several selected rotor positions*
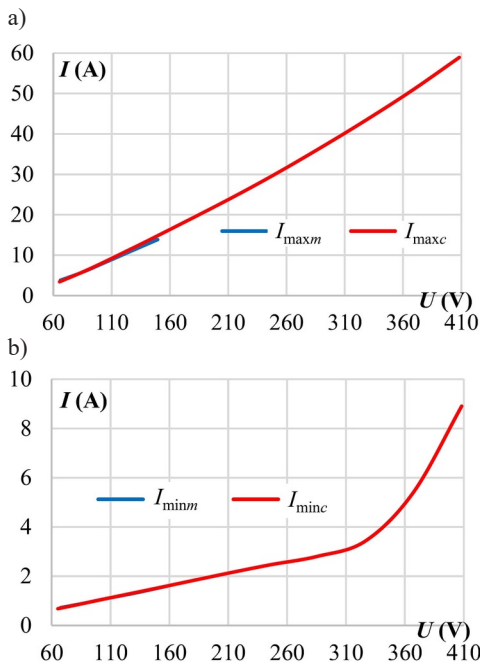
a)



b)



*Fig. 13. Currents (a) maximum and (b) minimum as a function of armature winding supply voltage determined during post-measurements ($I_{maxm}$, $I_{minm}$) and obtained by simulations ($I_{maxc}$, $I_{minc}$) at n = 1494 rpm*

lower computational effort (the calculation time for selected amplitude of phase current is about 15 minutes) such approach requires to find zero "slotting reluctance torque" position of the rotor and thus is less reliable than proposed low slip method. Despite lower reliability simplified "forced current" approach can be still useful at initial stage of the SynRM design process.

Proposed low slip method allow also to determine the impact of nonlinearity of the magnetic circuit on performance of the SynRM.

The FEA have been performed for supply voltage up to 410 V with step of 50 V. The determined by means of the numerical model dependencies of $I_{maxc}$, $I_{minc}$ shown in Figure 13 allows to calculate, according to proposed method, the direct axis *d* and the quadrature axis *q* inductances and reactances as a function of supply voltage – see Figure 14.
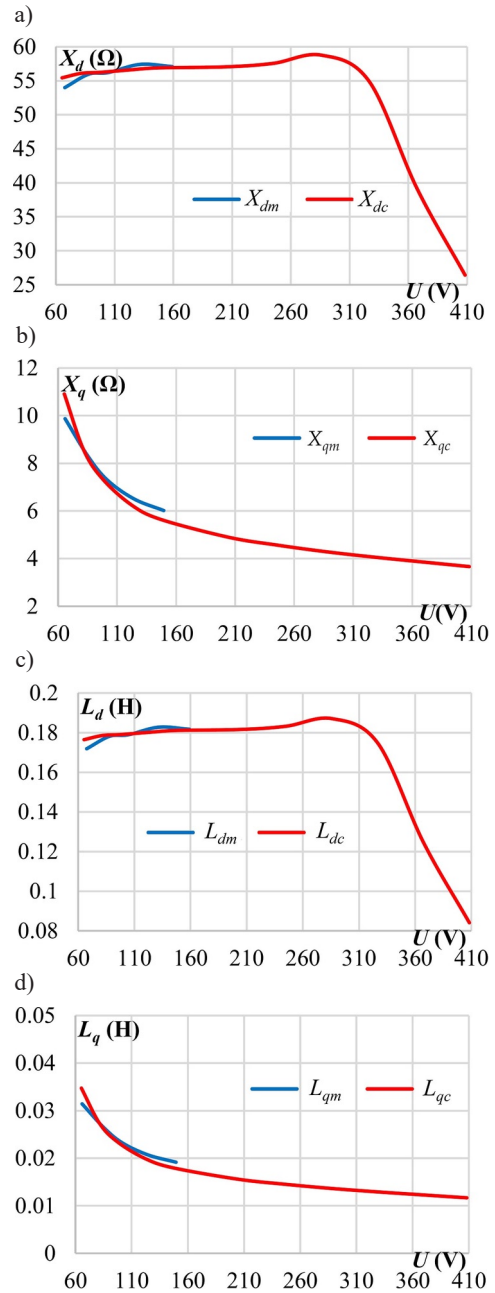
a)



b)



c)



d)



*Fig. 14. Reactances (a) direct $X_d$ and (b) quadrature $X_q$ and inductances (c) direct $L_d$ and quadrature (d) $L_q$ determined as a function of voltage U on the armature windings*

## 4. Conclusions

The presented contribution deals with analysis of performance of synchronous reluctance machine. An effective method for identifying the direct and quadrature inductances of SynRM based on measurements and finite element analysis of SynRM operation at low slip has been proposed and demonstrated on a case study problem. The proposed method takes into account nonlinearity of the magnetic circuit as well as the influence of the end winding leakage flux inductance. It should also be emphasized that in the proposed method the inductances are determined at a frequency close to the operational rated frequency.

An effective field model of SynRM was developed to determine the parameters of the equivalent circuit diagram. Such circuit models of parameters determined by means of the complex field models can be implemented in control systems to improve the functional performance of drive systems with SynRMs. The proposed field models can also be useful in the synthesis of reliable multiphase SynRMs.

In addition, a simplified "forced current" method allowing to determine torque-angle characteristics has been examined. The results obtained show that, despite the much lower computational complexity, this approach, due to the influence of stator slotting, may be useful only at the initial stage of the SynRM design process.

Studies related to the analysis of SynRM performance focused on the determination of power losses are ongoing and will be the scope of the further publications by the authors.

## References

1.  Agamloh E, von Jouanne A, Yokochi A. An Overview of Electric Machine Trends in Modern Electric Vehicles. Machines 2020; 8(2): 20, https://doi.org/10.3390/machines8020020.
2.  Arafat A, Islam Md Z, Tarek Md T B, Choi S. Transient Stability Comparison between Five-phase and Three-phase Permanent Magnet Assisted Synchronous Reluctance Motor. 2018 IEEE Transportation Electrification Conference and Expo (ITEC), 2018: 1–6, https://doi.org/10.1109/ITEC.2018.8450145.
3.  Baranski M. FE analysis of coupled electromagnetic-thermal phenomena in the squirrel cage motor working at high ambient temperature. COMPEL - The international journal for computation and mathematics in electrical and electronic engineering 2019; 38(4): 1120–1132, https://doi.org/10.1108/COMPEL-10-2018-0384.
4.  Baranski M, Szelag W, Lyskawinski W. An analysis of a start-up process in LSPMSMs with aluminum and copper rotor bars considering the coupling of electromagnetic and thermal phenomena. Archives of Electrical Engineering 2019; 68(4): 933–946, https://doi.org/10.24425/aee.2019.130693.
5.  Burlikowski W, Kielan P, Kowalik Z. Synchronous reluctance machine drive control with fast prototyping card implementation. Archives of Electrical Engineering 2020; 69(4): 757–769, https://doi.org/10.24425/aee.2020.134627.
6.  Chudzik A, Warda B. Fatigue life prediction of a radial cylindrical roller bearing subjected to a combined load using FEM. Eksploatacja i Niezawodnosc - Maintenance and Reliability 2020; 22(2): 212–220, https://doi.org/10.17531/ein.2020.2.4.
7.  Deng Y, Liu X, Udpa L. Magneto-Optic Imaging for Aircraft Skins Inspection: A Probability of Detection Study of Simulated and Experimental Image Data. IEEE Transactions on Reliability 2012; 61(4): 901–908, https://doi.org/10.1109/TR.2012.2221613.
8.  Garbiec T, Jagiela M. Accounting for Slot Harmonics and Nonsinusoidal Unbalanced Voltage Supply in High-Speed Solid-Rotor Induction Motor Using Complex Multi-Harmonic Finite Element Analysis. Energies 2021; 14(17): 5404, https://doi.org/10.3390/en14175404.
9.  Heidari H, Rassõlkin A, Kallaste A et al. A Review of Synchronous Reluctance Motor-Drive Advancements. Sustainability 2021; 13(2): 729, https://doi.org/10.3390/su13020729.
10. Ibrahim M, Allam Dr S, Rashad E E. Performance Improvement of a Photovoltaic Pumping System Using a Synchronous Reluctance Motor. Electric Power Components and Systems 2013; 41(4): 447–464, https://doi.org/10.1080/15325008.2012.749554.
11. Jagieła M, Gwóźdź J. Steady-state time-periodic finite element analysis of a brushless DC motor drive considering motion. Archives of Electrical Engineering 2015; 64(3): 471–486, https://doi.org/10.2478/aee-2015-0036.
12. Jedryczka C. Comparative analysis of the three- and six-phase fractional slot concentrated winding permanent magnet machines. COMPEL - The international journal for computation and mathematics in electrical and electronic engineering 2017; 36(3): 811–823, https://doi.org/10.1108/COMPEL-09-2016-0431.
13. Jędryczka C, Danielczyk D, Szeląg W. Torque Ripple Minimization of the Permanent Magnet Synchronous Machine by Modulation of the Phase Currents. Sensors 2020; 20(8): 2406, https://doi.org/10.3390/s20082406.
14. Jedryczka C, Szelag W, Lukaszewicz P. Analysis and Experimental Verification of Six-Phase Permanent Magnet Synchronous Machine Performance. 2018 International Symposium on Electrical Machines (SME), 2018: 1–4, https://doi.org/10.1109/ISEM.2018.8442684.
15. Kępczak N, Bechciński G, Rosik R. Experimental verification of the deep hole boring bar model. Eksploatacja i Niezawodnosc - Maintenance and Reliability 2021; 23(1): 55–62, https://doi.org/10.17531/ein.2021.1.6.
16. Knypiński Ł. Constrained optimization of line-start PM motor based on the gray wolf optimizer. Eksploatacja i Niezawodnosc - Maintenance and Reliability 2021; 23(1): 1–10, https://doi.org/10.17531/ein.2021.1.1.
17. Kurzawa M, Jędryczka C, Wojciechowski R M. Application of Multi-Branch Cauer Circuits in the Analysis of Electromagnetic Transducers Used in Wireless Transfer Power Systems. Sensors 2020; 20(7): 2052, https://doi.org/10.3390/s20072052.
18. Lipo T A. Synchronous Reluctance Machines-A Viable Alternative for AC Drives? Electric Machines & Power Systems 1991; 19(6): 659–671, https://doi.org/10.1080/07313569108909556.
19. Lopes H, Silva S P, Machado J. A simulation strategy to determine the mechanical behaviour of cork-rubber composite pads for vibration isolation. Eksploatacja i Niezawodnosc - Maintenance and Reliability 2021; 24(1): 80–88, https://doi.org/10.17531/ein.2022.1.10.
20. López-Torres C, Garcia-Espinosa A, Riba J-R. Reliable Design of PMaSynRM, IntechOpen: 2018: 105–128, https://doi.org/10.5772/intechopen.76355.
21. Ludowicz W, Wojciechowski R M. Analysis of the Distributions of Displacement and Eddy Currents in the Ferrite Core of an Electromagnetic Transducer Using the 2D Approach of the Edge Element Method and the Harmonic Balance Method. Energies 2021; 14(13): 3980, https://doi.org/10.3390/en14133980.
22. Lyskawinski, W. Comparative analysis of energy performance of squirrel cage induction motor, line-start synchronous reluctance and permanent magnet motors employing the same stator design. Archives of Electrical Engineering 2020; 69(4): 967–981, https://doi.org/10.24425/aee.2020.134642.
23. Lyskawinski W, Szelag W, Jedryczka C, Tolinski T. Finite Element Analysis of Magnetic Field Exciter for Direct Testing of Magnetocaloric Materials' Properties. Energies 2021; 14(10): 2792, https://doi.org/10.3390/en14102792.
24. Mahmoudi A, Kahourzade S, Roshandel E, Soong W L. Axial-Flux Synchronous Reluctance Motors: Introduction of a New Machine. 2020 IEEE International Conference on Power Electronics, Drives and Energy Systems (PEDES), 2020: 1–6, https://doi.org/10.1109/PEDES49360.2020.9379345.

25. Młot A, Kowol M, Kołodziej J et al. Analysis of IPM motor parameters in an 80-kW traction motor. Archives of Electrical Engineering 2020; 69(2): 467–481, https://doi.org/10.24425/aee.2020.133038.

26. Niazi P, Toliyat H A, Goodarzi A. Robust Maximum Torque per Ampere (MTPA) Control of PM-Assisted SynRM for Traction Applications. IEEE Transactions on Vehicular Technology 2007; 56(4): 1538–1545, https://doi.org/10.1109/TVT.2007.896974.

27. Oprea C, Dziechciarz A, Martis C. Comparative analysis of different synchronous reluctance motor topologies. 2015 IEEE 15th International Conference on Environment and Electrical Engineering (EEEIC), 2015: 1904–1909, https://doi.org/10.1109/EEEIC.2015.7165463.

28. Otomo Y, Igarashi H. Topology Optimization Using Gabor Filter: Application to Synchronous Reluctance Motor. IEEE Transactions on Magnetics 2021; 57(6): 1–4, https://doi.org/10.1109/TMAG.2021.3057402.

29. Ozcelik N G, Dogru U E, Imeryuz M, Ergene L T. Synchronous Reluctance Motor vs. Induction Motor at Low-Power Industrial Applications: Design and Comparison. Energies 2019; 12(11): 2190, https://doi.org/10.3390/en12112190.

30. Pałka R, Caramia R, Piotuch R. Multiobjective FEM based optimization of BLDC motor using Matlab and Maxwell scripting capabilities. Archives of Electrical Engineering 2014; 63(1): 115–124, https://doi.org/10.2478/aee-2014-0009.

31. Pałka R, Woronowicz K, Kotwas J et al. Influence of different supply modes on the performance of linear induction motors. Archives of Electrical Engineering 2019; 68(3): 473–483, https://doi.org/10.24425/aee.2019.129335.

32. Pellegrino G, Jahns T M, Bianchi N et al. The Rediscovery of Synchronous Reluctance and Ferrite Permanent Magnet Motors. 1st edition. Springer International Publishing: 2016. doi:10.1007/978-3-319-32202-5, https://doi.org/10.1007/978-3-319-32202-5.

33. Pop A-C, Pop Piglesan F, Martis R et al. First Insights on the Electromagnetic Design of Axial-Flux Synchronous-Reluctance Maschine. IECON 2018 - 44th Annual Conference of the IEEE Industrial Electronics Society, 2018: 5702–5709, https://doi.org/10.1109/IECON.2018.8591235.

34. Pop-Pîgleşan F, Pop A-C, Marţiş C. Synchronous Reluctance Machines for Automotive Cooling Fan Systems: Numerical and Experimental Study of Different Slot-Pole Combinations and Winding Types. Energies 2021; 14(2): 460, https://doi.org/10.3390/en14020460.

35. Przybylski M. Calculations and measurements of torque and inductance of switched reluctance motors with laminated and composite magnetic cores. Archives of Electrical Engineering 2022; 71(1): 125–138, https://doi.org/10.24425/aee.2022.140201.

36. Rezk H, Tawfiq K B, Sergeant P, Ibrahim M N. Optimal Rotor Design of Synchronous Reluctance Machines Considering the Effect of Current Angle. Mathematics 2021; 9(4): 344, https://doi.org/10.3390/math9040344.

37. Rodriguez J, Garcia C, Mora A et al. Latest Advances of Model Predictive Control in Electrical Drives—Part II: Applications and Benchmarking With Classical Control Methods. IEEE Transactions on Power Electronics 2022; 37(5): 5047–5061, https://doi.org/10.1109/TPEL.2021.3121589.

38. Stranz A, Szymański G, Bernat J et al. Infinite time horizon optimal current control of a stepper motor exploiting a finite element model. Bulletin of the Polish Academy of Sciences: Technical Sciences 2014; 62(4): 835–541, https://doi.org/10.2478/bpasts-2014-0092.

39. Sugiura O, Akiyama Y. Precise method for measuring Xd and Xq based on slip test of synchronous machines. Conference Record of the 1993 IEEE Industry Applications Conference Twenty-Eighth IAS Annual Meeting, 1993: 155–162 vol.1, https://doi.org/10.1109/IAS.1993.298918.

40. Sun J, Zheng Z, Li C et al. Optimal Fault-Tolerant Control of Multiphase Drives Under Open-Phase/Open-Switch Faults Based on DC Current Injection. IEEE Transactions on Power Electronics 2022; 37(5): 5928–5936, https://doi.org/10.1109/TPEL.2021.3135280.

41. Tawfiq K B, Ibrahim M N, EL-Kholy E E, Sergeant P. Performance Analysis of a Rewound Multiphase Synchronous Reluctance Machine. IEEE Journal of Emerging and Selected Topics in Power Electronics 2022; 10(1): 297–309, https://doi.org/10.1109/JESTPE.2021.3106591.

42. Tawfiq K B, Ibrahim M N, Sergeant P. An Enhanced Fault-Tolerant Control of a Five-Phase Synchronous Reluctance Motor Fed from a Three-to-Five-phase Matrix Converter. IEEE Journal of Emerging and Selected Topics in Power Electronics 2022: 1–1, https://doi.org/10.1109/JESTPE.2022.3148188.

43. Vagati A, Franceschini G, Marongiu I, Troglia G P. Design criteria of high performance synchronous reluctance motors. Conference Record of the 1992 IEEE Industry Applications Society Annual Meeting, 1992: 66–73, https://doi.org/10.1109/IAS.1992.244463.

44. Wang B, Wang J, Griffo A, Shi Y. Investigation Into Fault-Tolerant Capability of a Triple Redundant PMA SynRM Drive. IEEE Transactions on Power Electronics 2019; 34(2): 1611–1621, https://doi.org/10.1109/TPEL.2018.2834539.

45. Yang J W, Dai Z Y, Zhang Z. Modeling and fault diagnosis of multi-phase winding inter-turn short circuit for five-phase PMSM based on improved trust region. Microelectronics Reliability 2020; 114: 113778, https://doi.org/10.1016/j.microrel.2020.113778.

46. Yang Z, Shang F, Brown I P, Krishnamurthy M. Comparative Study of Interior Permanent Magnet, Induction, and Switched Reluctance Motor Drives for EV and HEV Applications. IEEE Transactions on Transportation Electrification 2015; 1(3): 245–254, https://doi.org/10.1109/TTE.2015.2470092.

47. Zdziebko P, Martowicz A. Study on the temperature and strain fields in gas foil bearings – measurement method and numerical simulations. Eksploatacja i Niezawodnosc - Maintenance and Reliability 2021; 23(3): 540–547, https://doi.org/10.17531/ein.2021.3.15.

48. Zdziebko P, Martowicz A, Uhl T. Multi-domain approach to modeling pantograph-catenary interaction. Eksploatacja i Niezawodnosc - Maintenance and Reliability 2022; 24(1): 130–139, https://doi.org/10.17531/ein.2022.1.15.

49. Zhang X-Y, Lu Z-H, Wu S-Y, Zhao Y-G. An Efficient Method for Time-Variant Reliability including Finite Element Analysis. Reliability Engineering & System Safety 2021; 210: 107534, https://doi.org/10.1016/j.ress.2021.107534.

50. Zhao F, Tian Z, Bechhoefer E, Zeng Y. An Integrated Prognostics Method Under Time-Varying Operating Conditions. IEEE Transactions on Reliability 2015; 64(2): 673–686, https://doi.org/10.1109/TR.2015.2407671.